ORIGINAL PAPER

An Analytical Investigation on the Nonlinear Vibration Behavior of a New Hybrid Laminated Nanocomposite Cylindrical Shell Resting on the Three-Parameter Nonlinear Substrate

Peng Zhang[1] · Zheng Meng[2] · Hui Wei[3] · Nhon Liu[3]

Abstract

Purpose The current analytical study is devoted to examining the nonlinear free vibration behavior of the laminated nanocomposite cylindrical shells containing multi-scale hybrid reinforcements once a nonlinear three-parameter substrate surrounds the structures. The multi-phase material of the structures includes polymeric matrix, nano-scale GOPs, which are uniformly distributed through the thickness of each layer and macro-scale carbon fibers with various orientation angles.

Methods The effective material properties of each multi-phase nanocomposite layer are calculated by implementing the modified Halpin–Tsai micromechanical scheme together with the extended rule of the mixture in a hierarchy. After that, with an incorporation of the improved Donnell's shell theory and Hamilton's principle, the governing equations are derived. Then by adopting a two-step solution technique, these nonlinear equations are transferred to one ordinary differential equation via Galerkins' method, and in the next step, the nonlinear frequencies of the structure are obtained by employing the multiple scale technique.

Results In the framework of various graphical results, a parametric analysis is conducted in detail to reveal the influences of the different parameters such as nonlinear foundation parameters, carbon fibers' orientation angles, GOPs' weight, and carbon fibers' volume fractions and length-to-radius ratios on the nonlinear vibration characteristics of the multi-phase laminated nanocomposite cylindrical shell.

Conclusions The results declare that the addition of the GO nanofillers along with the CFs and also embedding the structure on the nonlinear substrate can significantly enhance the vibrational behavior of the multi-phase laminated nanocomposite cylindrical shell.

Keywords Nonlinear vibration · Laminated cylindrical shell · Multi-scale reinforcements · Improved Donnell's shell theory · Multiple scale technique · Nonlinear substrate

Introduction

Today, composite materials are used in almost every industry in which stiffness and weight are important factors. Carbon fiber reinforced composites (CFRC) are kind of strong and lightweight composites utilized in our many daily life products. The CFRCs have some superiorities compared to traditional materials and other FRCs, such as metals and glass fiber-reinforced composites. These advantages include lighter weight, higher stiffness, and excellent performance in high temperatures [1, 2]. In these composites, the role of the polymer matrix is just to hold and protect fibers together and makes some toughness for these materials. According to the low capacity of the polymers in tolerating the loads, the polymer matrix has a slight contribution in the effective stiffness

✉ Zheng Meng
  2002mengzheng@163.com

1 Faculty of Architecture and Civil Engineering, Huaiyin Institute of Technology, Huaian 223001, Jiangsu, China

2 College of Applied Technology, Dalian Ocean University, Dalian 116300, Liaoning, China

3 School of Mechanical and Aerospace Engineering, Nanyang Technological University, 50 Nanyang Avenue, Singapore 639798, Singapore

of the CFRC structures. However, in recent years, scientists have introduced polymer nanocomposites with high stiffness and significant electrical, thermal, and mechanical properties, which can cover the most deficiency of the polymers. These polymer nanocomposites with improved features usually contain one of the evolved and advanced nanofillers such as graphene, graphene platelet (GPL), and carbon nanotube (CNT). Due to the outstanding mechanical properties, these polymer nanocomposites have been utilized in numerous industrial and general products such as fuel tanks, blades, packaging, fuel cell, energy sensors, etc. [3]. Undoubtedly, many theoretical, numerical, and experimental investigations have been conducted on these polymer nanocomposites to reveal their characteristics and capabilities for use in various industries. Some of these investigations are going to be reviewed in this section focusing on the theoretical analyses in the field of dynamic and static responses of the structures made of these materials. For the CNT-reinforced structures, Shen et al. [4] studied the effect of the thermal environment on the nonlinear vibration behavior of the polymer nanocomposite shells reinforced with various uniform and functionally graded (FG) patterns of single-walled CNTs through the thickness of the shells. Utilizing the first-order shear deformation theory (FSDT) with Donnell's shell assumptions and von Kármán nonlinearities was utilized by Mirzaei et al. [5] to survey the buckling analysis of the CNT reinforced conical shells in the presence of thermal loading. Heydarpour et al. [6] considered consideration the effect of Coriolis and centrifugal forces in the investigation dealing with the natural frequency responses of the FG-CNT reinforced conical shells by implementing Hamilton's principle based on the FSDT. Heydari et al. [7] procured a nonlinear theoretical model to solve the bending problem of the embedded temperature-dependent polymer nanocomposite plate reinforced with graded CNTs through the thickness based on the Mindlin plate theory coupled with Hamilton's principle. A semi-analytical approach was employed by Chakraborty et al. [8] in order to examine the mechanical responses of the laminated FG-CNT reinforced cylindrical nanocomposite shells by adopting the higher-order shear deformation theory (HSDT) in the framework of vibration, post-buckling, and buckling analyses. Avramov et al. [9] presented a finite-degree-of-freedom model to include the geometrical nonlinearities effects in the research relating to the vibration characteristics of the CNT-reinforced nanocomposite shells once a supersonic flow is applied to the structures. Also, on the basis of FSDT, the issue of the vibration analysis of the conical, cylindrical polymeric shells and annular polymeric plates containing single-walled CNTs as reinforcement was investigated by Qin et al. [10] with the aid of the unified Fourier series solution. Most recently, Liew et al. [11] have successfully predicted the both static and dynamic behaviors of the CNT-reinforced nanocomposite

cylindrical panels according to the 3D elasticity theory by applying the axial and circumferential initial stresses to the structures. Also, the nonlinear transient vibration behavior of the magneto-electro-elastic material reinforced with CNTs has been examined by Mahesh [12] based on the finite element method. Moreover, some new recent and exciting researches have been devoted to analyze the wave propagation and vibration mode shapes of CNTs [13, 14].

Graphene and GPLs are two of the other carbon-based nanofillers with great potential to be employed in numerous applications such as energy storage, MEMS and NEMS devices, cells, etc., owing to their astounding thermal, electrical, mechanical, and optical properties [15–17]. Besides, one of the other applications of graphene and GPLs relating to this research is that they can be terrific nanoscale reinforcements in high-strength polymer nanocomposites [18–20]. The reason is that they have excellent stiffness and strength [21, 22] and also better compatibility with polymers in comparison with CNTs due to their large surface area which can interact with carbon chains more effectively. The properties of graphene and GPLs make them ideal nano reinforcements, and they have recently been used in various investigations related to the mechanical behavior of reinforced polymer nanocomposite structures. For instance, a numerical solution technique by the name "generalized differential quadrature method (GDQM)" was implemented by Shen et al. [23] to find out the nonlinear-to-linear natural frequencies of the embedded thermally affected graphene-reinforced laminated beams based on the HSDT. Li et al. [24] developed a computational investigation on the dynamic stability and nonlinear vibration responses of the sandwich plates consisting of two metal face sheets and a porous GPL reinforced nanocomposite while various external effects such as thermal environment, damping, and elastic substrate had also been regarded. Newly, Ye et al. [25] solved the forced vibration problem of the GPL-reinforced metal foam nanocomposite shells in which the ordinary differential governing equations were achieved via nonlinear Donnell's shell theory and then solved according to the pseudo-arclength continuation numerical method.

Although graphene is a perfect nanofiller for reinforcing polymers, its process to be synthesized is very time-consuming and exhaustive which needs high accuracy and full-time attention. Consequently, the final product would be very expensive. Graphene oxide (GO) is a derivative of graphene obtained from the exfoliation of graphite oxide through a low-cost process [26]. Moreover, GO can cause a strong interaction with many polymers [27] due to the presence of these oxygen-containing groups which leads to perfect load transfer between the fillers and matrix. These features bring about the GO to be an extraordinary nanofiller for polymer nanocomposites. In comparison with CNTs, graphene oxide powders (GOPs) showed better improvement

in mechanical analyses. With this regard, Zhang et al. [28] compared the dynamic and static responses of the GOP and CNT-reinforced nanocomposite beams with each other by utilizing FSDT and then proved that GOPs had better performance in these analyses. Thereafter, Ebrahimi et al. [29–33] analytically studied the static and dynamic behavior of the GOP-reinforced nanocomposite structures in employing developed a hypothesis with the name of refined higher-order shear deformation theory. Also, Wang et al. [34] probed the nonlinear static behavior of the FG-GOP reinforced micro arches with regarding the von Kármán geometrical nonlinearities based on the exponential shear deformation theory incorporated with a couple stress-based model. The literature review demonstrates that there are only a few limited papers that examined the mechanical responses of the GOP-reinforced nanocomposite structures.

Although, the aforesaid macro-fiber reinforced composites and polymer nanocomposites with nanofillers exhibit improved material properties; recently, scientists introduced a novel type of nanocomposites that profit from both macro- and nanoscale reinforcements. These kinds of reinforcements are called multi-scale hybrid reinforcements. Still, there are few works that can be found in the literature that analyzed the mechanical behavior of these novel types of nanocomposites. Zarei et al. [35] and Hajmohammad et al. [36] illustrated the influence of hygrothermal environments on the dynamic instability region of the laminated conical shells consisting of multi-phase material with macro- and nanoscale reinforcements while the viscoelastic properties and magnetic field were regarded in their works, respectively. Free vibration and wave propagation analyses of the monolayer multi-scale hybrid nanocomposite structures were carried out by Ebrahimi et al. [37–40] by employing the Halpin–Tsai micromechanical model and taking into consideration the effect of fibers' orientation angle on the frequency responses. A combination of the Eshelby–Mori–Tanaka method and Han's homogenization method was considered by Yousefi et al. [41] to estimate the material properties of the multi-phase CNT/fiber/polymer laminated conical shells to numerically analyze the free vibration behavior of these multi-scale hybrid structures. A parametric study on the geometrically nonlinear dynamic behavior of the CNT/fiber/polymer multi-scale hybrid nanocomposite cylindrical panels was conducted by Lee [42], considering delamination around a central cutout. Most recently, Shahmohammadi et al. [43] performed an analytical study on the dynamic instability of the general nanocomposite shells consisting of three phases of polymer, CNT and fibers, once the structures were subjected to pressure and thermal loadings via an isogeometric approach. According to the literature survey and to best of the authors' knowledge, there are no studies concerning the three-phase nanocomposites containing GO nanoparticles and macro-scale carbon fibers as multi-scale

hybrid reinforcements in the framework of the four-layer laminated shell structures.

In this paper, the nonlinear free vibration behavior of the embedded four-layer laminated nanocomposite cylindrical shells consisting of a polymeric matrix, nano GOPs, and macro-scale carbon fibers is perused through an analytical study. This stiff nanocomposite benefits from both astounding properties of GO nanofillers and macro-scale CFs, and by changing the CFs' orientation angles, the stiffness of this hybrid material can be tailorable for specific applications. Then, a modified version of Donnell's nonlinear shell theory is employed to define the strains of the proposed structure in terms of displacement components. Afterward, on the basis of Hamilton's principle, the nonlinear governing equations are derived and then solved by means of multiple-scale solution techniques to obtain the nonlinear vibration responses of the proposed structures. Finally, some new findings have been achieved by investigating the influences of the critical parameters such as fibers' orientation angle, GOPs' weight fraction, foundation parameters, etc., which have never been discussed before.

Theory and Formulation

Materials Homogenization Process

In the present research, a three-phased material is utilized in the proposed cylindrical shell containing an epoxy matrix and two types of carbon-based nano-size and macro-size reinforcements. It is worth mentioning that the graphene oxide (GO) nanofillers are scattered uniformly through the thickness of the structure, but the carbon fibers (CFs) can be added in a favorable orientation angle to reach the desirable type of laminate. These constituents are composed to construct a laminated multi-scale hybrid nanocomposite cylindrical shell structure.

Then, to attain the effective mechanical characteristics of the aforementioned three-phased nanocomposite material, in the first step, the Halpin–Tsai micro-mechanical homogenization procedure is utilized to obtain Young's modulus of the GOR nanocomposite according to the following set of hierarchical equations [28]:

$$E_{GORNC} = 0.49E_l + 0.51E_t \tag{1}$$

In the preceding equation, E_{GORNC} belongs to the equivalent Young's modulus of the GOR nanocomposite and also E_l and E_t are the longitudinal and transverse Young's modulus of the mentioned nanocomposite, respectively. Henceforth, the subscript *GORNC* refers to the GOR nanocomposite. Also, the E_l and E_t can be expressed as below:

$$E_l = E_M \times \left(\frac{1 + \xi_l \eta_l V_{GO}}{1 - \eta_l V_{GO}} \right), \quad E_t = E_M \times \left(\frac{1 + \xi_t \eta_t V_{GO}}{1 - \eta_t V_{GO}} \right) \tag{2}$$

where the subscripts *M* and *GO* refer to the epoxy matrix and GO nanoparticles, respectively. Moreover, the other parameters which are used in the above equation but are not defined before are calculated in the following:

$$\eta_l = \left(E_{GO}/E_M - 1 \right) / \left(E_{GO}/E_M + \xi_l \right), \\ \eta_t = \left(E_{GO}/E_M - 1 \right) / \left(E_{GO}/E_M + \xi_t \right) \tag{3}$$

where ξ_l and ξ_t denote the geometry factors that can be defined utilizing d_{GO} and h_{GO} which belongs to the GO powders' diameter and thickness, respectively, as below [28]:

$$\xi_l = \xi_t = 2 \, d_{GO}/h_{GO} \tag{4}$$

Thereupon, it is imperative to express the way of obtaining the equivalent mass density (ρ), Poisson's ratio (ν), and the bulk moduli (K) of the GOR nanocomposite, which are attained by implementing the rule of mixture homogenization method, as given below:

$$\nu_{GORNC} = \nu_{GO} V_{GO} + \nu_M V_M \tag{5}$$

$$\rho_{GORNC} = \rho_{GO} V_{GO} + \rho_M V_M \tag{6}$$

$$K_{GORNC} = \frac{E_{GORNC}}{3 \times (1 - 2\nu_{GORNC})} \tag{7}$$

where *V* represents the volume fraction of the relevant subscript.

Furthermore, the following equation can be used to obtain the epoxy matrix volume fraction:

$$V_M = 1 - V_{GO} \tag{8}$$

where the total volume fraction of reinforcements (V_{GO}) can be expressed using the weight fraction of GOs' (W_{GO}) and the mass density of GOs and epoxy matrix together, as follows:

$$V_{GO} = \frac{W_{GO}}{W_{GO} + \rho_{GO}(1 - W_{GO})/\rho_M} \tag{9}$$

Then, Hooke's law is employed to obtain the equivalent shear moduli of GOR nanocomposite (G_{GORNC}), as expressed below:

$$G_{GORNC} = \frac{E_{GORNC}}{2(1 + \nu_{GORNC})} \tag{10}$$

Hitherto, the effective material properties of the GOR nanocomposite have been achieved by implementing a set of Hierarchical equations. But, as discussed before, the final proposed material consisted of three phases including the embedded macro-size CFs into the GOR nanocomposite material. Hence, it is acceptable to consider the GOR nanocomposite material as the matrix for the final three-phased hybrid nanocomposite material. Accordingly, it is time to start using proper equations to find the effective material properties of the aforementioned final multi-scale hybrid nanocomposite. In this regard, the extended rule of the mixture is employed to obtain the effective characteristics of the mentioned orthotopic multi-scale hybrid nanocomposite material, as given in the following [44]:

$$E_{eff}^{11} = V_{CF} E_{CF}^{11} + V_{GORNC} E_{GORNC} \tag{11}$$

$$\frac{1}{E_{eff}^{22}} = \frac{1}{E_{CF}^{22}} + \frac{V_{GORNC}}{E_{GORNC}} + V_{CF} V_{GORNC} \\ - \frac{\left(\dfrac{\nu_{CF}^2 E_{GORNC}}{E_{CF}^{22}} + \dfrac{\nu_{GORNC}^2 E_{CF}^{22}}{E_{GORNC}} - 2\nu_{CF}\nu_{GORNC} \right)}{\dfrac{1}{V_{CF} E_{CF}^{22} + V_{GORNC} E_{GORNC}}} \tag{12}$$

$$\frac{1}{G_{eff}^{12}} = \frac{V_{CF}}{G_{CF}^{12}} + \frac{V_{GORNC}}{G_{GORNC}} \tag{13}$$

$$\rho_{eff} = V_{CF} \rho_{CF} + V_{GORNC} \rho_{GORNC} \tag{14}$$

$$\nu_{eff}^{12} = V_{CF} \nu_{CF} + V_{GORNC} \nu_{GORNC} \tag{15}$$

where the CF subscript belongs to the carbon fibers' properties. Moreover, the following equation correlates the volume fraction of the carbon fibers and the GOR nanocomposite:

$$V_{GORNC} + V_{CF} = 1 \tag{16}$$

Hitherto, the effective material properties of the presented hybrid multi-scale composite, comprising CFs macro-scale and GOs nano-scale reinforcements, have been achieved by the means of Eqs. (11)-(15). In the following, we intend to achieve the motion equations of the vibrational behavior of the laminated nanocomposite shells embedded on the non-linear elastic foundation.

Governing Equations

The proposed cylindrical shell is composed of three-phase laminated material with length *L*, mean radius *R*, and a wall thickness of *h*, which is schematically depicted in Fig. 1. Also,

Fig. 1 Geometry, forces, and stress resultants and coordinate system of the laminated hybrid nanocomposite cylindrical shell
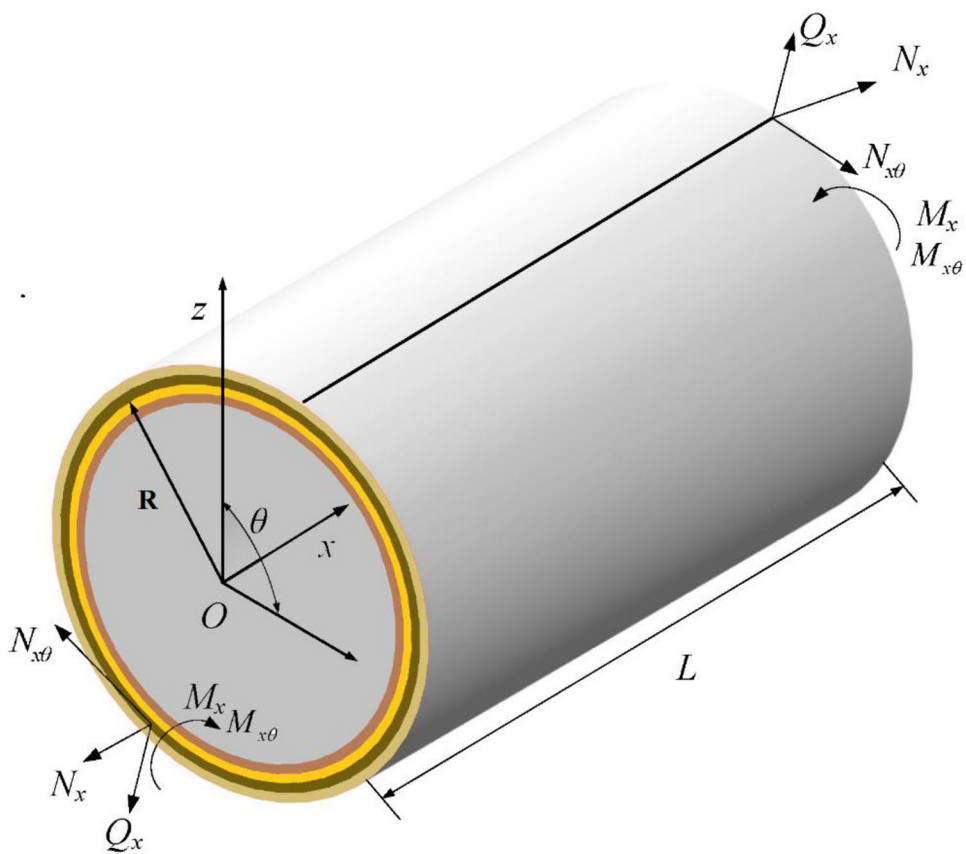
this figure shows that the x-θ-z coordinate system in which the axes are selected in the longitudinal, circumferential, and inward normal to the middle plane directions, respectively, is located on the middle surface of the left end. As mentioned earlier, the proposed structure is embedded in the three-parameter nonlinear foundation. To introduce the foundation parameters, including K_L, K_S, and K_{NL}, Fig. 2 is provided, in which the red color represents the proposed cylindrical shell shown in Fig. 1. According to the defined coordinate system, u, v, and

w belong to the displacements of the arbitrary points in the middle plane of the aforementioned shell along the x-, θ-, and z- axis directions, respectively. Now, the displacement fields of the presented model can be obtained by implementing the Kirchhoff–Love hypothesis as below [45]:

$$u_x(x, \theta, z, t) = u(x, \theta, t) - z \frac{\partial}{\partial x} W(x, \theta, t) \tag{17}$$
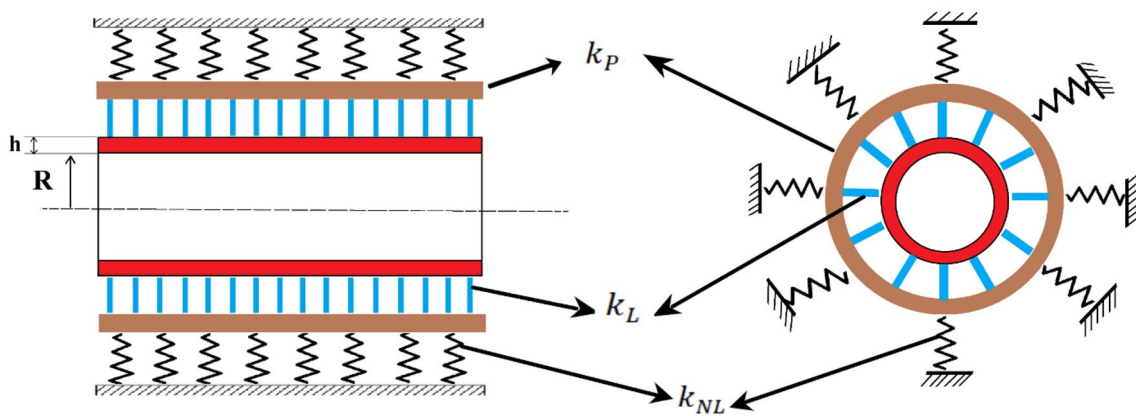
Fig. 2 Schematic of the laminated nanocomposite cylindrical shell resting on a three-parameter nonlinear substrate

$$u_y(x, \theta, z, t) = v(x, \theta, t) - (z/R)\frac{\partial}{\partial \theta}W(x, \phi, t) \tag{18}$$

$$u_z(x, \theta, z, t) = w(x, \theta, t) \tag{19}$$

where t and z denote the time variable and the distance of the arbitrary point of the laminated shell from the middle surface.

It should be noted that for the designated laminated cylindrical shell, the constitutive relationship between stresses and strains can be formed as below [46]:

$$\begin{bmatrix} \sigma_{xx}^k \\ \sigma_{\theta\theta}^k \\ \tau_{x\theta}^k \end{bmatrix} = \begin{bmatrix} \overline{Q}_{11} & \overline{Q}_{12} & 0 \\ \overline{Q}_{12} & \overline{Q}_{22} & 0 \\ 0 & 0 & \overline{Q}_{66} \end{bmatrix} \begin{bmatrix} \varepsilon_{xx} \\ \varepsilon_{\theta\theta} \\ \varepsilon_{x\theta} \end{bmatrix} \tag{20}$$

where,

$$\begin{aligned} \overline{Q}_{11} &= Q_{11}\cos^4\theta + Q_{22}\sin^4\theta + 2Q_{12}\sin^2\theta\cos^2\theta \\ \overline{Q}_{22} &= Q_{11}\sin^4\theta + Q_{22}\cos^4\theta + 2Q_{12}\sin^2\theta\cos^2\theta \\ \overline{Q}_{12} &= \frac{1}{4}\sin^2 2\theta(Q_{11} + Q_{22}) + Q_{12}(\sin^4\theta + \cos^4\theta) \\ \overline{Q}_{66} &= Q_{66}\cos^2\theta \end{aligned} \tag{21}$$

Thereinto, θ belongs to the carbon fibers' orientation angle in kth layer of the proposed laminated multi-phase composite, and Q parameters can be defined as follows:

$$Q_{11} = \frac{E_{eff}^{11}}{1 - \nu_{12}\nu_{21}}, \quad Q_{22} = \frac{E_{eff}^{22}}{1 - \nu_{12}\nu_{21}}, \quad Q_{12} = \frac{\nu_{12}E_{eff}^{22}}{1 - \nu_{12}\nu_{21}}, \quad Q_{66} = E_{eff}^{12} \tag{22}$$

Moreover, the nonlinear strain–displacement equations based on the Kirchhoff–Love theory, for the cylindrical shell must be written in the following form [46]:

$$\begin{aligned} \varepsilon_{xx} &= \varepsilon_{x,0} + z\kappa_{xx} \\ \varepsilon_{\theta\theta} &= \varepsilon_{\theta,0} + z\kappa_{\theta\theta} \\ \gamma_{x\theta} &= \gamma_{x\theta,0} + 2z\kappa_{x\theta} \end{aligned} \tag{23}$$

In which, the $\varepsilon_{x,0}$, $\varepsilon_{y,0}$, and $\gamma_{x\theta,0}$ belong to the middle-plain strains. Also, κ_{xx}, $\kappa_{\theta\theta}$, and $\kappa_{x\theta}$ denote the middle surface curvature and torsions.

It is worth mentioning that Donnell's nonlinear shell theory confronts imprecision at the small circumferential wavenumber. Hence, it has been decided to utilize the improved Donnell's nonlinear shell hypothesis to overcome the aforementioned imprecision. Accordingly, the related expressions in the before equations can be represented as follows:

$$[\varepsilon_{x,0}, \varepsilon_{\theta,0}, \gamma_{x\theta,0}] = \left[\frac{1}{2}\left(2\frac{\partial u}{\partial x} + (\frac{\partial w}{\partial x})^2\right), \frac{w}{R} + \frac{1}{R}\left(\frac{\partial v}{\partial \theta} + \frac{1}{2R}(\frac{\partial w}{\partial \theta})^2\right), \frac{1}{R}\left(\frac{\partial u}{\partial \theta} + \frac{\partial w}{\partial x}\frac{\partial w}{\partial \theta}\right) + \frac{\partial v}{\partial x}\right] \tag{24}$$

$$[\kappa_{xx}, \kappa_{\theta\theta}, \kappa_{x\theta}] = \left[\frac{-\partial^2 w}{\partial x^2}, \frac{-1}{R^2}\frac{\partial}{\partial \theta}\left(\frac{\partial w}{\partial \theta} - v\right), \frac{-1}{R}\frac{\partial}{\partial x}\left(\frac{\partial w}{\partial \theta} - v\right)\right] \tag{25}$$

The internal moment and force resultants are given by the following equations:

$$\begin{aligned} [N_x \, M_x] &= \int_{-h/2}^{h/2}[1 \; z]\,\sigma_{xx}^k\,dz \\ [N_\theta \, M_\theta] &= \int_{-h/2}^{h/2}[1 \; z]\,\sigma_{\theta\theta}^k\,dz \\ [N_{x\theta} \, M_{x\theta}] &= \int_{-h/2}^{h/2}[1 \; z]\,\tau_{x\theta}^k\,dz \end{aligned} \tag{26}$$

Thus, by substituting Eqs. (20) and (23) into Eq. (26), it yields the constitutive equations in the matrix form as follows [46, 47]:

$$\begin{Bmatrix} N_x \\ N_\theta \\ N_{x\theta} \\ M_x \\ M_\theta \\ M_{x\theta} \end{Bmatrix} = \begin{bmatrix} A_{11} & A_{12} & 0 & B_{11} & B_{12} & 0 \\ A_{12} & A_{22} & 0 & B_{12} & B_{22} & 0 \\ 0 & 0 & A_{66} & 0 & 0 & B_{66} \\ B_{11} & B_{12} & 0 & D_{11} & D_{12} & 0 \\ B_{12} & B_{22} & 0 & D_{12} & D_{22} & 0 \\ 0 & 0 & B_{66} & 0 & 0 & D_{66} \end{bmatrix} \begin{Bmatrix} \varepsilon_{x,0} \\ \varepsilon_{\theta,0} \\ \gamma_{x\theta,0} \\ \kappa_x \\ \kappa_\theta \\ 2\kappa_{x\theta} \end{Bmatrix} \tag{27}$$

Thereinto,

$$[A_{ij}, B_{ij}, D_{ij}] = \sum_{k=1}^{N=4}\int_{z_k}^{z_{k+1}}\overline{Q}_{ij}[1, z, z^2]\,dz, \; i, j = 1, 2, 6 \tag{28}$$

Now, Hamilton's principle [48] will be utilized as below for obtaining the Euler–Lagrange equations:

$$\int_{t_1}^{t_2}\delta(\Pi_K - \Pi_S - \Pi_F)dt = 0 \tag{29}$$

Then, at this stage, it is required to express the strain energy Π_S, kinetic energy Π_K, and the work done by the external forces Π_F. To define these parameters, we have [49]:

$$\begin{aligned} \delta\Pi_S &= \int_V \sigma_{ij}^k\delta\varepsilon_{ij}dV \\ &= \int_0^{2\pi}\int_0^L \left(N_x\varepsilon_{x,0} + N_{x\theta}\gamma_{x\theta,0} + N_\theta\varepsilon_{\theta,0} + M_x\kappa_{xx} + M_{x\theta}\kappa_{x\theta} + M_\theta\kappa_{\theta\theta}\right) \\ &\quad Rdxd\theta \end{aligned} \tag{30}$$

$$\delta\Pi_K = \frac{1}{2}\int_0^L\int_0^{2\pi}\rho_{eff}^T\left(\left(\frac{\partial u}{\partial t}\right)^2 + \left(\frac{\partial v}{\partial t}\right)^2 + \left(\frac{\partial w}{\partial t}\right)^2\right)Rd\theta dx \tag{31}$$

$$\delta\Pi_F = \frac{1}{2}\int_0^L\int_0^{2\pi}\left(k_L w - k_P\left(\left(\frac{\partial^2 w}{\partial x^2}\right) + \left(\frac{\partial^2 w}{R^2\partial\theta^2}\right)\right) + k_{NL}w^3\right)Rdxd\theta \tag{32}$$

In Eq. (31) ρ_{eff}^T is the total mass density of the structure which can be defined as follows:

$$\rho_{eff}^T = \sum_{k=1}^{N=4}\int_{z_k}^{z_{k+1}}\rho_{eff}^k dz \tag{33}$$

Also, the external forces in Eq. (32) include just the forces related to the three-parameter nonlinear elastic foundation and there are no other external forces in this study. In this regard, k_L, k_P, and k_{NL} are the parameters of the linear sublayer, shear layer, and nonlinear springs, respectively.

By substituting Eqs. (30)-(32) in Eq. (29), and then putting the coefficients of δu, δv, and δw equal to zero, the following nonlinear Euler–Lagrange equations of the proposed model can be obtained as given below:

$$\frac{\partial N_{x\theta}}{R\partial\theta} + \frac{\partial N_x}{\partial x} = \rho_{eff}^T\frac{\partial^2 u}{\partial t^2} \tag{34}$$

$$\frac{\partial M_\theta}{R^2\partial\theta} + \frac{2\partial M_{x\theta}}{R\partial x} + \frac{\partial N_\theta}{R\partial\theta} + \frac{\partial N_{x\theta}}{\partial x} = \rho_{eff}^T\frac{\partial^2 v}{\partial t^2} \tag{35}$$

$$\frac{N_\theta}{R}\left(\frac{\partial^2 W}{\partial\theta^2} - 1\right) + 2N_{x\theta}\frac{\partial^2 w}{R\partial x\partial\theta} + N_x\frac{\partial^2 w}{\partial x^2} + \frac{\partial w}{R\partial\theta}\left(\frac{\partial N_\theta}{\partial\theta} + \frac{\partial N_{x\theta}}{\partial x}\right) + \frac{\partial w}{\partial x}\left(\frac{\partial N_x}{\partial x} + \frac{\partial N_{x\theta}}{R\partial\theta}\right)$$
$$+ \frac{\partial^2 M_\theta}{R^2\partial\theta^2} + \frac{\partial^2 M_x}{\partial x^2} + 2\frac{\partial^2 M_{x\theta}}{R\partial x\partial\theta} - k_L w + k_P\left(\frac{\partial^2 w}{\partial x^2} + \frac{\partial^2 w}{R^2\partial\theta^2}\right) + k_{NL}w^3 = \rho_{eff}^T\frac{\partial^2 w}{\partial t^2} \tag{36}$$

Afterward, by introducing Eqs. (27) and (28) into Eqs. (34, 35, 36), it yields:

$$A_{11}\left(\frac{\partial^2 u}{\partial x^2} + \frac{\partial^2 w}{\partial x^2}\frac{\partial w}{\partial x}\right) + \frac{A_{12}}{R}\left(\frac{\partial^2 v}{\partial x\partial\theta} + \frac{\partial w}{\partial x}\left(1 + \frac{\partial^2 w}{\partial x\partial\theta}\right)\right) +$$
$$\frac{A_{66}}{R^2}\left(\frac{\partial^2 u}{\partial\theta^2} + \frac{R\partial^2 v}{\partial x\partial\theta} + \frac{\partial w}{\partial x}\frac{\partial^2 w}{\partial\theta^2} + \frac{\partial w}{\partial\theta}\frac{\partial^2 w}{\partial x\partial\theta}\right) = \rho_{eff}^T\frac{\partial^2 u}{\partial t^2} \tag{37}$$

$$\frac{A_{11}}{R^2}\left(\frac{\partial^2 v}{\partial\theta^2} + \frac{\partial w}{\partial\theta}\left(1 + \frac{\partial^2 w}{R\partial\theta^2}\right)\right) + \frac{A_{12}}{R^2}\left(\frac{R\partial^2 u}{\partial x\partial\theta} + \frac{\partial^2 w}{\partial x\partial\theta}\frac{\partial w}{\partial\theta}\right) +$$
$$\frac{A_{66}}{R}\left(\frac{\partial^2 u}{\partial x\partial\theta} + R\frac{\partial^2 v}{\partial x^2} + \frac{\partial^2 w}{\partial x\partial\theta}\frac{\partial w}{\partial x} + \frac{\partial^2 w}{\partial x^2}\frac{\partial w}{\partial\theta}\right) = \rho_{eff}^T\frac{\partial^2 v}{\partial t^2} \tag{38}$$

$$\frac{A_{11}}{R}\left(\frac{\partial v}{\partial\theta} + \frac{1}{2R}\left(\frac{\partial w}{\partial\theta}\right)^2 + w\right) - \frac{A_{12}}{R}\left(\frac{\partial u}{\partial x} + \frac{1}{2}\left(\frac{\partial w}{\partial x}\right)^2\right)$$
$$- D_{11}\left(\frac{\partial^4 w}{\partial x^4} + \frac{\partial^4 w}{R^4\partial\theta^4}\right)$$
$$- \frac{2D_{12}}{R^2}\frac{\partial^4 w}{\partial x^2\partial\theta^2} - \frac{4D_{66}}{R^2}\frac{\partial^4 w}{\partial x^2\partial\theta^2} - k_L w$$
$$+ k_P\left(\frac{\partial^2 w}{\partial x^2} + \frac{\partial^2 w}{\partial\theta^2}\right) - k_{NL}w^3 + P_1 + P_2 = \rho_{eff}^T\frac{\partial^2 w}{\partial t^2} \tag{39}$$

where P_1 and P_2 correspond with:

$$P_1 = \frac{A_{12}}{R^2}\frac{\partial^2 w}{\partial\theta^2}\left(\frac{\partial u}{\partial x} + \frac{1}{2}\left(\frac{\partial w}{\partial x}\right)^2\right)$$
$$+ \frac{A_{12}}{R}\frac{\partial w}{\partial\theta}\left(\frac{\partial^2 u}{\partial x^2} + \frac{\partial w}{\partial x}\frac{\partial^2 w}{R\partial x\partial\theta}\right)$$
$$+ A_{11}\frac{\partial w}{\partial x}\left(\frac{\partial^2 u}{\partial x^2} + \frac{\partial w}{\partial x}\frac{\partial^2 w}{\partial x^2}\right)$$
$$+ \frac{A_{11}}{R^3}\left(\frac{\partial v}{\partial\theta} + \frac{1}{2R^2}\left(\frac{\partial w}{\partial\theta}\right)^2 + w\right)$$
$$+ \frac{A_{11}}{R^2}\frac{\partial w}{\partial\theta}\left(\frac{\partial^2 v}{R\partial\theta^2} + \frac{\partial w}{\partial\theta}\frac{\partial^2 w}{R^2\partial\theta^2} + \frac{\partial w}{R\partial\theta}\right)$$
$$+ A_{11}\frac{\partial^2 w}{\partial x^2}\left(\frac{\partial u}{\partial x} + \left(\frac{\partial w}{\partial x}\right)^2\right)$$
$$+ \frac{A_{12}}{R}\frac{\partial w}{\partial x}\left(\frac{\partial^2 v}{\partial x\partial\theta} + \frac{\partial w}{\partial\theta}\frac{\partial^2 w}{R\partial x\partial\theta} + \frac{\partial w}{\partial x}\right)$$
$$+ \frac{A_{12}}{R}\frac{\partial^2 w}{\partial x^2}\left(\frac{\partial v}{\partial\theta} + \frac{1}{2R}\left(\frac{\partial w}{\partial\theta}\right)^2 + w\right) \tag{40}$$

$$P_2 = \frac{A_{66}}{R^2}\frac{\partial w}{\partial\theta}\left(\frac{\partial^2 u}{\partial x\partial\theta} + R\frac{\partial^2 v}{\partial x^2} + \frac{\partial^2 w}{\partial x^2}\frac{\partial w}{\partial\theta} + \frac{\partial w}{\partial x}\frac{\partial^2 w}{\partial x\partial\theta}\right)$$
$$+ \frac{2A_{66}}{R^2}\frac{\partial^2 w}{\partial x\partial\theta}\left(\frac{\partial u}{\partial\theta} + R\frac{\partial v}{\partial x} + \frac{\partial w}{\partial x}\frac{\partial w}{\partial\theta}\right)$$
$$+ \frac{A_{66}}{R}\frac{\partial w}{\partial x}\left(\frac{\partial^2 u}{R\partial\theta^2} + \frac{\partial^2 v}{\partial x\partial\theta} + \frac{\partial^2 w}{\partial x\partial\theta}\frac{\partial w}{R\partial\theta} + \frac{\partial w}{R\partial x}\frac{\partial^2 w}{\partial\theta^2}\right) \tag{41}$$

Also, the corresponding general boundary conditions are concurrently attained as follows:

$$x = 0, L \text{ then } \begin{cases} \delta u = 0, \text{ or } N_x = 0 \\ \delta v = 0, \text{ or } 2M_{x\theta} + RN_{x\theta} = 0 \\ \delta w = 0, \text{ or } \frac{N_x\partial w}{\partial x} + \frac{N_{x\theta}\partial w}{R\partial\theta} + \frac{\partial M_x}{\partial x} + \frac{2\partial M_{x\theta}}{\partial\theta} = 0 \\ M_x = 0, \text{ or } \delta(\partial w/\partial x) = 0 \end{cases} \tag{42}$$

$$\theta = 0, 2\pi \text{ then} \begin{cases} \delta u = 0, \text{ or } N_{x\theta} = 0 \\ \delta v = 0, \text{ or } M_\theta + RN_\theta = 0 \\ \delta w = 0, \text{ or } \dfrac{N_\theta \partial w}{\partial \theta} + \dfrac{N_{x\theta} \partial w}{\partial x} + \dfrac{\partial M_\theta}{R \partial \theta} + \dfrac{2 \partial M_{x\theta}}{\partial x} = 0 \\ M_\theta = 0, \text{ or } \delta(\partial w/\partial \theta) = 0 \end{cases}$$

$$(43)$$

Solution Procedure

By considering the implemented simply supported boundary conditions, at $x = 0$ and also $x = L$ the relations given below must be satisfied:

$$v = w = 0 \text{ and } \frac{\partial u}{\partial x} = N_x = \frac{\partial^2 w}{\partial x^2} = M_x = 0 \tag{44}$$

Accordingly, the displacement functions that can satisfy the aforementioned boundary condition, by considering the m and n as the axial half-wave number and circumferential wave number, respectively, can be set as below:

$$u(x, \theta, t) = \sum_{m=1}^{\infty} \sum_{n=1}^{\infty} u_{mn}(t) \cos(m\pi x/L) \cos(n\theta) \tag{45}$$

$$v(x, \theta, t) = \sum_{m=1}^{\infty} \sum_{n=1}^{\infty} v_{mn}(t) \sin(m\pi x/L) \sin(n\theta) \tag{46}$$

$$w(x, \theta, t) = \sum_{m=1}^{\infty} \sum_{n=1}^{\infty} w_{mn}(t) \sin(m\pi x/L) \cos(n\theta) \tag{47}$$

where $u_{mn}(t)$, $v_{mn}(t)$, and $w_{mn}(t)$ belong to the displacement amplitude components.

Also, by substituting Eqs. (45), (46) and (47) into Eqs. (37), (38) and (39) and then employing Galerkin's method, we can achieve the subsequent set of ordinary differential equations:

$$\tilde{L}_{11} u_{mn}(t) + \tilde{L}_{12} v_{mn}(t) + \tilde{L}_{13} w_{mn}(t) + \tilde{L}_{14} w_{mn}^2(t) = \ddot{u}_{mn}(t) \tag{48}$$

$$\tilde{L}_{21} u_{mn}(t) + \tilde{L}_{22} v_{mn}(t) + \tilde{L}_{23} w_{mn}(t) + \tilde{L}_{24} w_{mn}^2(t) = \ddot{v}_{mn}(t) \tag{49}$$

$$\begin{aligned} &\tilde{L}_{31} u_{mn}(t) + \tilde{L}_{32} v_{mn}(t) + \tilde{L}_{33} w_{mn}(t) + \tilde{L}_{34} u_{mn}(t) w_{mn}(t) \\ &+ \tilde{L}_{35} v_{mn}(t) w_{mn}(t) + \tilde{L}_{36} w_{mn}^2(t) + \tilde{L}_{37} w_{mn}^3(t) = \ddot{w}_{mn}(t) \end{aligned} \tag{50}$$

in which the coefficients $\tilde{L}_{ij}(i, j = 1,2,...,7)$ given in the Appendix A.

According to the fact that two of the inertia terms $\ddot{u}_{mn}(t)$ and $\ddot{v}_{mn}(t)$, compared with the transverse inertia term $\ddot{w}_{mn}(t)$ have inconsiderable effects, then both can be neglected in

Eqs. (48) and (49). Hence, by solving $u_{mn}(t)$ and $v_{mn}(t)$ in the aforesaid equations, and also substituting the results in Eq. (50) we have:

$$\ddot{w}_{mn}(t) + a_1 w_{mn}(t) + a_2 w_{mn}^2(t) + a_3 w_{mn}^3(t) = 0 \tag{51}$$

By considering the following initial conditions:

$$w_{mn}(t = 0) = w_{max}, \frac{\partial w_{mn}}{\partial t}\Big|_{t=0} = 0 \tag{52}$$

where w_{max} belongs to the maximum value of $w_{mn}(t)$.

Then, in order to solve Eq. (51), the multiple scale method is implemented. At first, it's required to present the scaled time by introducing a small dimensionless parameter named ε that has been used as a bookkeeping device, as given below:

$$T_\eta = \varepsilon^\eta t, \ \eta = 0, 1, 2, ... \tag{53}$$

Now, the time derivatives can be written in terms of T_η as below:

$$\begin{cases} \dfrac{\partial}{\partial t} = D_0 + \varepsilon D_1 + \varepsilon^2 D_2 \\ \dfrac{\partial^2}{\partial t^2} = (D_0)^2 + 2\varepsilon D_0 D_1 + \varepsilon^2 \left((D_1)^2 + 2 D_0 D_2 \right) \end{cases} \tag{54}$$

where

$$D_\eta \Big|_{\eta=0,1,2,...} = \frac{\partial}{\partial T_\eta} \tag{55}$$

The vibration response which is a function of various scaled times can be represented as follows:

$$\begin{aligned} w_{mn}(t) = {}& \varepsilon w_1(T_0, T_1, T_2, ...) + \varepsilon^2 w_2(T_0, T_1, T_2, ...) \\ &+ \varepsilon^3 w_3(T_0, T_1, T_2, ...) \end{aligned} \tag{56}$$

By introducing Eqs. (54)-(56) in Eq. (51) and also putting the coefficients of all powers of ε equal to zero, it yields:

$$(D_0^2 + \omega_0^2) w_1 = 0 \tag{57}$$

$$(D_0^2 + \omega_0^2) w_2 = -w_1(2 D_0 D_1 + a_2 w_1) \tag{58}$$

$$(D_0^2 + \omega_0^2) w_3 = -w_1(2 D_0 D_2 + a_3 w_1^2 + D_1^2 + 2 a_2 w_2) - 2 D_0 D_1 w_2 \tag{59}$$

In which, the achieved linear natural frequencies are achieved as follows:

$$\omega_0 = \omega_L = \sqrt{a_1} \tag{60}$$

Hence, for Eq. (57) the solution achieved as:

$$w_1 = A(T_1, T_2) \exp(i\omega_0 T_0) + \overline{A}(T_1, T_2) \exp(-i\omega_0 T_0)$$

(61)

Then by inserting it into Eq. (57) we obtain:

$$w_2(D_0^2 + \omega_0^2) = -2i\omega_0 A D_1 \exp(i\omega_0 T_0) - a_2 A^2 \exp(2i\omega_0 T_0)$$
$$- a_2 A\overline{A} + CC$$

(62)

where the CC term can be dedicated to the conjugate function of all former parameters.

Due to the elimination of all the secular terms in Eq. (62) we achieve:

$$w_2 = \frac{a_2}{3\omega_0} \exp(2i\omega_0 T_0) A^2 - \frac{a_2}{\omega_0^2} A\overline{A} + CC$$

(63)

By inserting w_1 and w_2 which have been found in Eqs. (61) and (63) into Eq. (59) we obtain:

$$w_3(D_0^2 + \omega_0^2) = -A^3 \left(a_3 + \frac{2a_2^2}{3\omega_0^2} \right) \exp(3i\omega_0 T_0) +$$
$$\overline{A}A^2 \left(-3a_3 + \frac{10a_2^2}{3\omega_0^2} - 2i\omega_0 D_2 / \overline{A}A \right) \exp(i\omega_0 T_0) + CC$$

(64)

Likewise, the secular terms in this equation must be omitted too:

$$-3a_3 \overline{A}A^2 + \frac{10a_2^2}{3\omega_0^2} \overline{A}A^2 - 2i\omega_0 D_2 A = 0$$

(65)

The solution of the above equation would be in the following form:

$$A = 0.5a \exp(i\psi)$$

(66)

By introducing the solution namely Eq. (66) in Eq. (65), we achieved a complex equation. Then by separating imaginary and real parts, we have:

$$\begin{cases} \omega_0 \dfrac{\partial a}{\partial T_2} = 0 \\ \dfrac{5a_2^2}{12\omega_0^2} a^3 - \dfrac{3a_3}{8} a^3 + \omega_0 a \dfrac{\partial \psi}{\partial T_2} = 0 \end{cases}$$

(67)

By solving Eq. (67) and assuming ψ_0 as a constant parameter, we attain:

$$\psi = T_2 a^2 \left(\frac{3a_3 \omega_0^2}{8\omega_0^3} - \frac{5a_2^2}{12\omega_0^3} \right) + \psi_0$$

(68)

By substituting Eqs. (67) and (52) into Eq. (65) the following equation can be attained:

$$A = \frac{a}{2} \exp\left(ia^2 \eta^2 t \left(\frac{3a_3 \omega_0^2}{8\omega_0^3} - \frac{5a_2^2}{12\omega_0^3} \right) + i\psi_0 \right)$$

(69)

Then, by substituting Eqs. (61), (63), and (69) in Eq. (56) we achieved the following relation:

$$w_{mn}(t) = \varepsilon a \cos(\omega_{NL} t + \psi_0)$$
$$- \frac{\varepsilon^2 a_2 a^2}{2a_1} \left(1 - \frac{1}{3} \cos(2\omega_{NL} t + 2\psi_0) \right) + O(\varepsilon^3)$$

(70)

Then we can obtain $a_1, a_2,$ and a_3 parameters as it is given below:

$$a_1 = \tilde{L}_{23} \frac{\tilde{L}_{12}\tilde{L}_{31} - \tilde{L}_{11}\tilde{L}_{32}}{\tilde{L}_{12}\tilde{L}_{21} - \tilde{L}_{23}\tilde{L}_{22}} - \tilde{L}_{22} \frac{\tilde{L}_{31}\tilde{L}_{13} - \tilde{L}_{11}\tilde{L}_{33}}{\tilde{L}_{12}\tilde{L}_{21} - \tilde{L}_{23}\tilde{L}_{22}}$$
$$+ \tilde{L}_{21} \frac{\tilde{L}_{32}\tilde{L}_{13} - \tilde{L}_{12}\tilde{L}_{33}}{\tilde{L}_{12}\tilde{L}_{21} - \tilde{L}_{23}\tilde{L}_{22}}$$

(71)

$$a_2 = 0$$

(72)

$$a_3 = \tilde{L}_{35}$$

(73)

By exerting the initial conditions into Eq. (52) we have:

$$\psi_0 = 0, \text{ and } a\varepsilon = w_{\max}$$

(74)

Eventually, the nonlinear frequency of the multi-phase laminated nanocomposite shell is achieved as:

$$\omega_{NL} = \sqrt{a_1} \left[1 + \varepsilon^2 a^2 \left(\frac{3a_3 a_1}{8a_1^2} - \frac{5a_2^2}{12a_1^2} \right) \right] + O(\varepsilon^3)$$

(75)

Table 1 Comparison of the linear natural frequencies (ω_L) of the thin isotropic cylindrical shell for different mode numbers

Mode numbers (m,n)	Linear natural frequencies, ω_L (Hz)			
	Ref [50]	Ref [51]	Ref [4]	Present
(1,7)	305.22	305.32	306.73	306.3423
(1,8)	281.31	281.37	281.30	282.3169
(1,9)	288.24	288.28	290.59	289.2502
(1,10)	317.49	317.51	320.04	318.5885
(1,11)	362.20	362.22	364.83	363.4435
(1,12)	417.94	417.96	420.59	419.3724
(1,13)	482.22	482.23	484.84	483.8618
(1,14)	553.67	553.67	556.24	555.5564
(1,15)	631.58	631.59	634.08	633.7257

Table 2 Comparison of the nonlinear to linear frequency ratio (ω_{NL}/ω_L) of the isotropic cylindrical shell with considering $w_{max}/h = 1$

Obtained from	(m,n)		
	(1,2)	(1,3)	(1,4)
Ref [52]	1.008	1.0060	1.0398
Ref [53]	1.0010	1.0064	1.0404
Present	1.009	1.0033	1.0117

Verification Studies

The nonlinear and linear frequency responses of the current study are compared with both experimental and numerical results of the previous works, investigating the vibrational performance of the cylindrical shell structures, to prove the accuracy and correctness of the present methodology.

A set of comparisons have been carried out in Table 1, in which the linear natural frequencies of a thin homogenous cylindrical shell have been obtained using various methods and theories such as improved Donnell's nonlinear shell theory (present study), finite element method (by Gonçalves et al. [50]), Sanders' shell theory (by Dym [51]), and HSDT (by Shen et al. [4]). The physical and geometrical parameters of this isotropic shell are considered as:

$$E = 210\,\text{Gpa}, \upsilon = 0.3, \rho = 7850\,\frac{\text{kg}}{\text{m}^3}, L = 410\,\text{mm}, h = 1\,\text{mm},$$

$R = 301.5\,\text{mm}.$ Comparing the results of this study in Table 1, with those reported in the other mentioned references, with considering different mode numbers, shows a perfect agreement and the result are quite close to each other.

In order to investigate the reliability of the nonlinear responses, the nonlinear-to-linear natural frequency ratios of an isotropic cylindrical shell are gathered in Table 2, with constant values of axial half-wave number (*m*) and variable values of circumferential wave number (*n*). As observed in this table, the very low differences between the results of this study and those reported by Raju et al. [52] and Rafiee et al. [53] can approve the accuracy of the present solution technique utilized for predicting the nonlinear frequencies.

Up to now, the validity of the various parts of this study, including theory and solution technique, related to the linear and nonlinear responses of the cylindrical shells, have been surveyed. To cover all parts of this investigation, the validity of the approach considered for the lamination concept of this paper is going to be asked in the framework of Table 3. In this table, the dimensionless linear natural frequencies of the cross-ply laminated nanocomposite cylindrical shells are compared with those provided by Chakraborty et al. [8] regarding various radius-to-thickness ratios and different CNTs' volume fractions. Again, an excellent agreement is obtained in this table.

This section revealed the high accuracy of the current methodology, and also it is confirmed that this study can competently predict the nonlinear vibration responses of the laminated nanocomposite cylindrical shells containing multi-scale reinforcements.

Numerical Results and Discussion

This section is allocated to survey the achieved results in the framework of graphical diagrams and tabulated outcomes by working on the nonlinear free vibration analysis of the

Table 3 Comparison of the dimensionless linear natural frequencies ($\Omega = \omega_L \left(\frac{L^2}{h}\right)\sqrt{\frac{\rho_m}{E_m}}$) of the cross-ply CNTR laminated [0/90/90/0] nanocomposite cylindrical shell with a uniform distribution pattern of CNTs

$\frac{R}{L}$	V_{CNT}					
	0.11		0.14		0.17	
	Present	Ref [8]	Present	Ref [8]	Present	Ref [8]
2	26.5580	26.5322	28.4251	28.3170	30.1294	29.9671
5	21.0253	20.9522	23.2095	23.0035	25.1261	24.8521
12	20.0466	19.9075	22.3163	22.0278	24.3057	23.9257

Table 4 Material properties of the multi-scale hybrid nanocomposite shell [28, 44]

Polymeric matrix (epoxy)	$E = 3\,\text{Gpa}, \upsilon = 0.34, \rho = 1200\,\text{kg/m}^3$
Graphene Oxide nanofillers (GOPs)	$E = 444.8\,\text{Gpa}, \upsilon = 0.165, \rho = 1090\,\text{kg/m}^3$
Carbon fibers (CFs)	$E_{11} = 233.05\,\text{Gpa}, E_{122} = 23.1\,Gpa, \upsilon = 0.2, \rho = 1750\,\text{kg/m}^3$

cross-ply laminated nanocomposite cylindrical shell, containing multi-scale hybrid reinforcements and, embedded on a three-parameter nonlinear foundation. The major center of attention in this segment would be on the susceptibility of the linear and nonlinear natural frequency responses versus the variations in some of the effective and important parameters, such as circumferential wave number, vibration amplitude, values of CF's volume fraction, and GOP's weight fraction, nonlinear three-parameter substrate (discrepancy applied on all three parameters together, or one by one individually), length-to-radius ratio, and also fibers' orientation angle. Also, in all illustrated graphs, the simultaneous effect of two or more parameters' variations is presented to help to reach a more extensive study. Furthermore, in terms of material characterization and finding the best and most optimized kind of material composition of multi-scale reinforcements, different types and percentages of macroscale CFs and nanoscale GOPs reinforcements is inspected through some plots. The material properties of the utilized reinforcements and polymer matrix are available in Table 4. It should be mentioned that the geometrical and other effective parameters would be as follows unless otherwise stated:

$$h = 0.002R, \; L = 20R, \; m = 1, \; n = 3, \; w_{max}/h = 1,$$
$$V_{CF} = 0.1, \; W_{Gop} = 1\%, \; K_{NL} = K_P = K_L = 0$$

Also, the radius (R) of the shell is considered to be 1 m in all tables and figures. In terms of perusing the variation of the nonlinear to linear frequency ratio due to applying changes in the circumferential wave number, Fig. 3, with three subplots, is depicted for different values of the vibration amplitude; each subplot consists of three branches indicating various amounts of the GOPs' weight fraction. It is observable that, in all three subplots, the values of the nonlinear to linear frequency ratio are experiencing an increasing trend up to reaching a particular maximum value, and then decrease suddenly with a declining slope, and tend to a constant value gradually. Furthermore, an enhancement in the percentage of the weight fraction of added GOP reinforcements, which causes an improvement in the stiffness of the matrix of the multi-scale hybrid nanocomposite, leads to the reduction in the nonlinear to linear frequency ratio, in all values of circumferential wave number or vibration amplitude. Also, as it is obvious, an improvement in the structure's stiffness induces an increment in the linear frequency parameter. But, the observed reduction in the nonlinear to linear frequency ratio values is probably due to the lower enhancement in the nonlinear frequency amounts compared to the linear frequency values. In addition, at any given circumferential wave number, by the increment of the vibration amplitude, values of the nonlinear to linear frequency ratio enhance in all GOP reinforcements' weight fraction amounts.

Figure 4 is plotted to investigate the influence of various values of the nonlinear three-parameter foundation on the nonlinear to linear frequency ratio at any given value of the vibration amplitude parameter, consisting of three independent graphs presented for different values of the CFs volume fraction. It can be seen that each branch of every graph experiences an increasing trend, which means the values of the nonlinear to linear frequency ratio are enhanced by the vibration amplitude's increment, which happens due to the direct relation. Also, it can be noticed that, at any given value of the vibration amplitude, regardless of the CFs' volume fraction, values of the nonlinear to linear frequency ratio lessen by enhancing the amounts of the nonlinear three-parameter foundation. Plus, this is worth mentioning that, the more the value of the CFs volume fraction grows, the more the branches of graphs become distinguished. This conversion appears since the nonlinear three-parameter foundation parameters increase, which leads to a growth in the stiffness characteristic of the proposed nanocomposite. Also, more detailed information about how each layer of this three-layered nonlinear substrate affects the nonlinear vibrational responses of the structure can be found in the results of the next figure. Further, as explained before, the growth of stiffness leads to a decrement in the nonlinear to linear frequency ratio. Moreover, it should be remarked that, by an increment in the percentage of CFs' volume fraction, all branches of different substrate parameters, confront a reduction in the nonlinear to linear frequency ratio values. In addition, the observed decline in the nonlinear to linear frequency ratio owing to the growth of the V_{CF} happens for a similar logic that has been explained previously via the observed reduction in the nonlinear to linear frequency ratio due to the increment of W_{GOP}.

The influence of embedding the structure on each layer of this nonlinear substrate individually versus the nonlinear to linear frequency ratio is illustrated in different subplots in Fig. 5. Besides, each subplot is devoted to exploring the effect of various values of the vibration amplitude too. It is clear that while the linear and nonlinear substrate parameters are subjected to an incrementation, the nonlinear to linear frequency ratio will experience decline and rise, respectively, linearly with a small slope. Although in the shear substrate parameter type, the nonlinear declining trend is observable, which means by increasing the values of the shear substrate parameter, the nonlinear to linear frequency ratio will reduce in a relatively severe trend. In addition, in each branch of subplots, it is evident that at any given value of the foundation parameters, applying an enhancement in the vibration amplitude value leads to an increment in the nonlinear to linear frequency ratio. Besides, in all subplots of this figure, especially in part (c), it can be seen that by employing some higher values of the vibration amplitude parameter, values of the nonlinear to linear frequency ratio
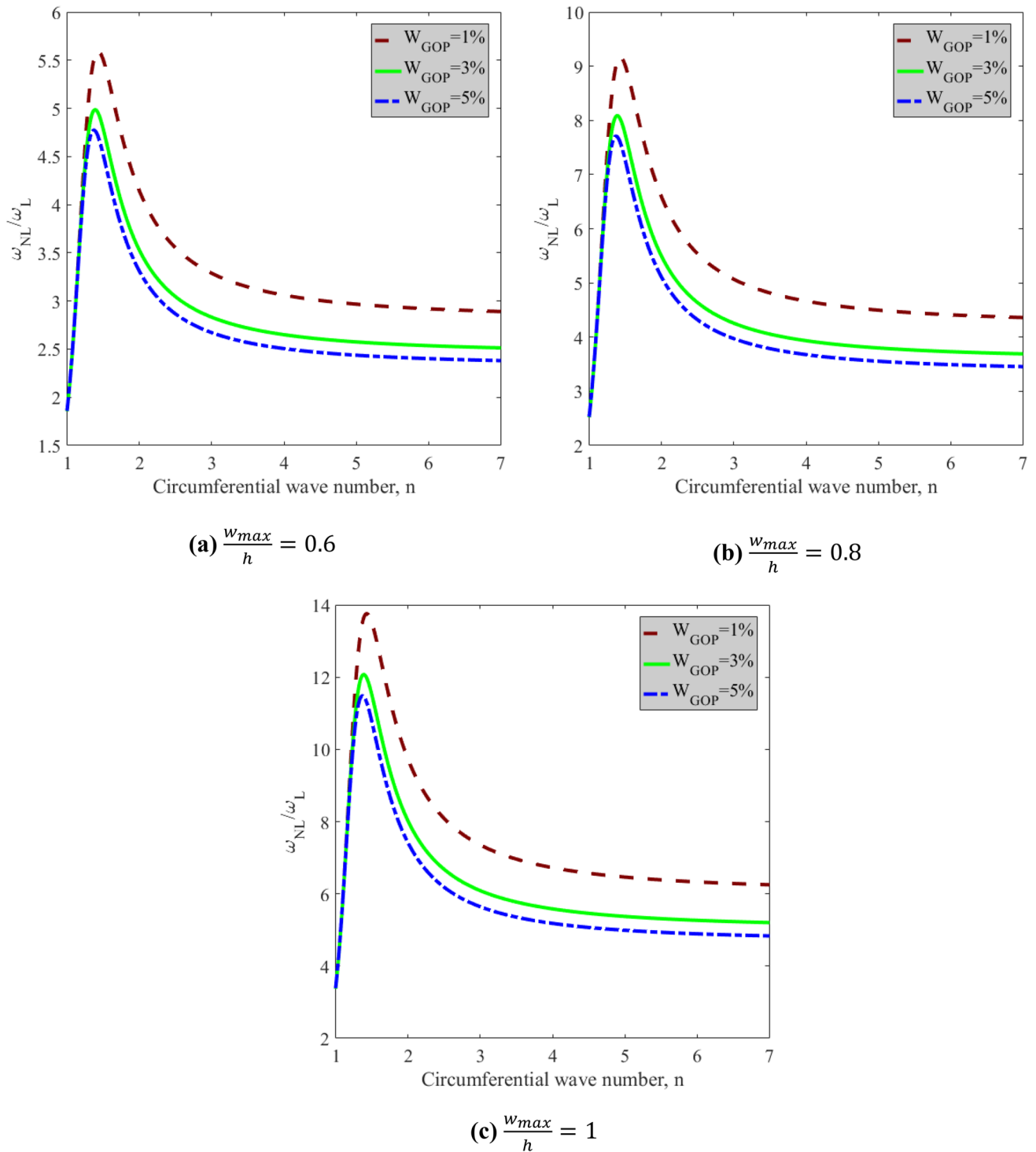
(a) $\frac{w_{max}}{h} = 0.6$

(b) $\frac{w_{max}}{h} = 0.8$

(c) $\frac{w_{max}}{h} = 1$

Fig. 3 Variation of the nonlinear to linear frequency ratio versus circumferential wave number for different values of vibration amplitude (w_{max}/h) and various amounts of GOPs ($m=1$, $V_{CF} = 0.1$)

will experience a steeper reduction in comparison with lower vibration amplitudes. In addition, in this group of graphs, it can be discovered that the shear foundation parameter has a more distinct influence on the variation trend of the nonlinear to linear frequency ratio.

Figure 6 is devoted to studying the effect of the fibers' orientation angle parameter on the nonlinear to linear frequency

(a) $V_{CF} = 0.1$

(b) $V_{CF} = 0.3$

(c) $V_{CF} = 0.5$
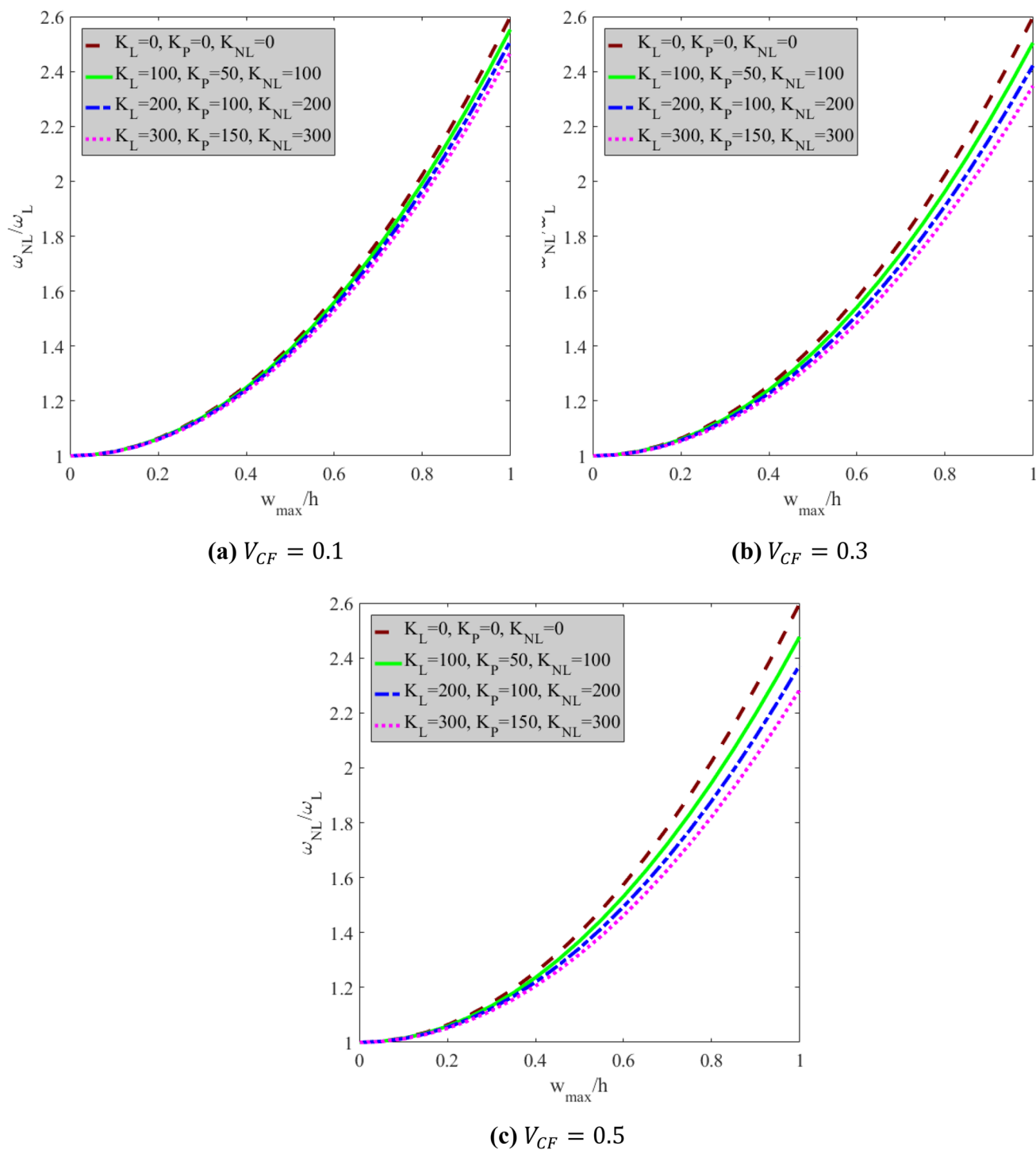
Fig. 4 Influence of nonlinear three-parameter substrate on the frequency ratio-amplitude curves with respect to various values of CFs' volume fractions ($n = 3$, $m = 1$, $W_{GOP} = 1\%$)

ratio, considering different values of the length-to-radius ratio via each branch of every subplot. In which, the influence of various amounts of the circumferential wave number is checked in different subplots. It is demonstrated that the nonlinear to linear frequency ratios values experience an

increasing–decreasing graph. Hence, certainly there exists a peak, this peak occurs at the 90-degree orientation angle, and then the trend starts to decline again till it tends to a constant value symmetrically. It is notable that regardless of the length-to-radius ratio, all the branches confront their

(a) Effect of linear sublayer ($K_P = K_{NL} = 0$)

(b) Effect of nonlinear springs ($K_P = K_L = 0$)

(c) Effect of shear layer ($K_L = K_{NL} = 0$)
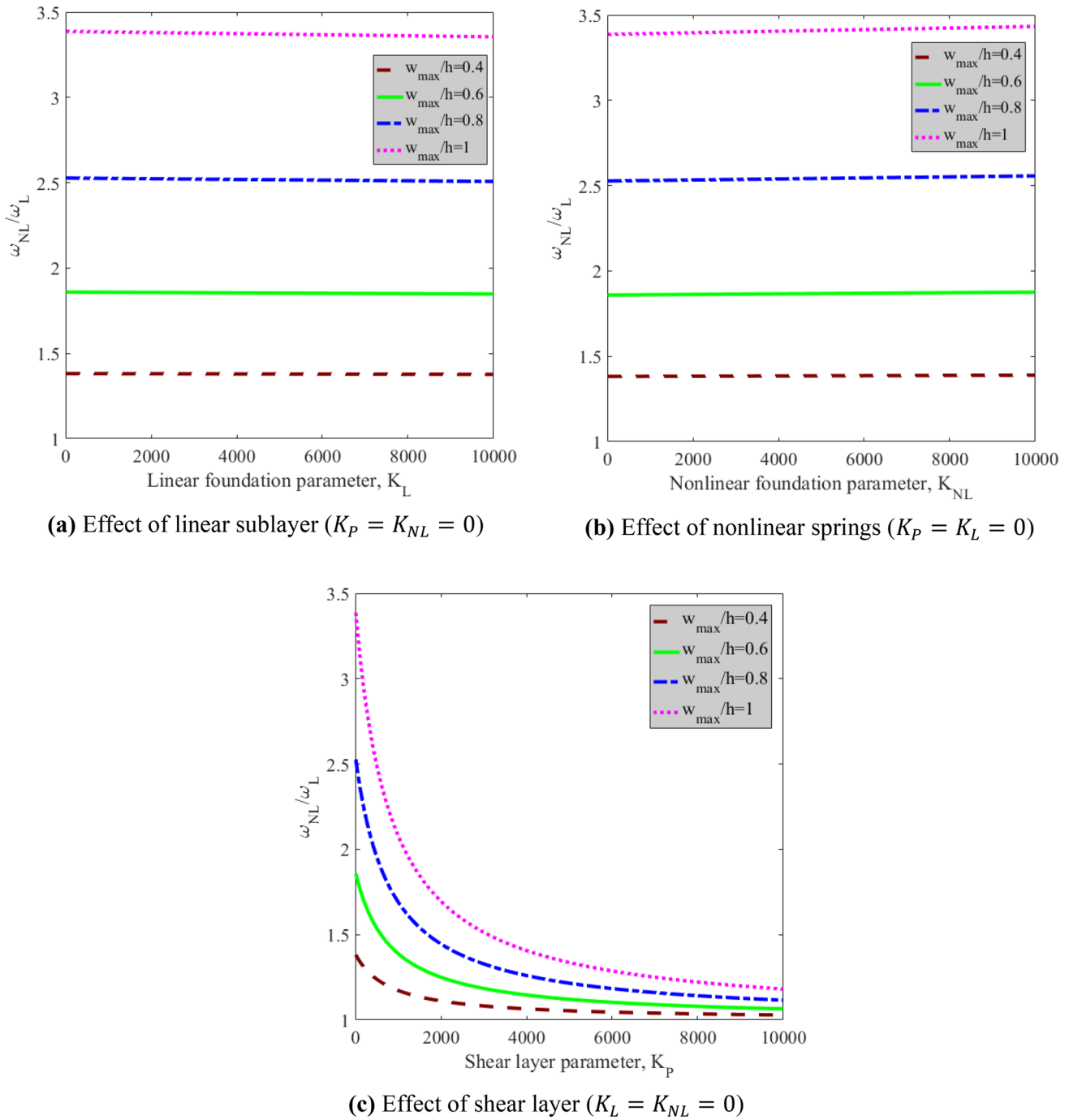
Fig. 5 Interaction of each layer of the nonlinear substrate with the hybrid laminated nanocomposite cylindrical shell with considering different values of vibration amplitude ($m = 1, n = 1, W_{GOP} = 3\%, V_{CF} = 0.1$)

maximum value of the nonlinear to linear frequency ratio at the 90-degree fibers' orientation angle. Furthermore, at any given value of the fibers' orientation angle, the increment of the length-to-radius ratio causes the enhancement of the nonlinear to linear frequency ratio parameter's values. Moreover, it's demonstrated that by applying an increase in the circumferential wave number's values, the nonlinear to linear

frequency ratios values increase, but after passing n = 2, this value confronts a reduction. It is worth mentioning that the foresaid response is valid according to the explored information in Fig. 3 before, which confirms that the nonlinear to linear frequency ratio values grow to a maximum value and then decrease afterward to reach a constant value. In addition, it is declared in the diagram that applying a decrement

(a) n=1

(b) n=2

(c) n=3
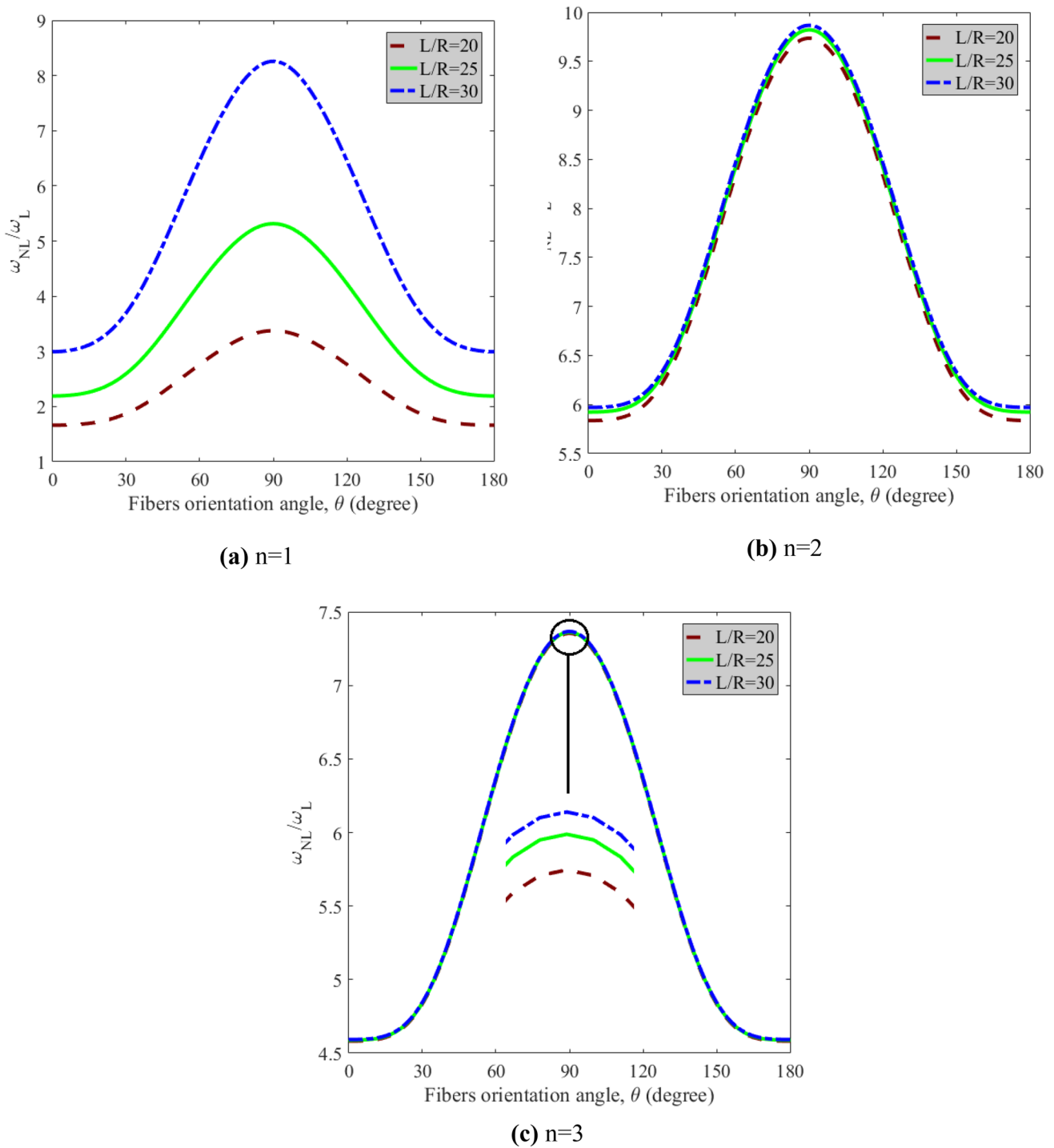
Fig. 6 Variation of the nonlinear to linear frequency ratio against CFs' orientation angle with considering different length-to-radius ratios for various circumferential wave numbers ($m = 1$, $W_{GOP} = 1\%$, $V_{CF} = 0.1$, $w_{max}/h = 1$)

in the circumferential wave number's values causes the branches of different values of the length-to-radius ratio get more distinguishable.

The simultaneous effects of the length-to-radius ratio and the GOPs' weight fraction on the nonlinear vibration responses of the structure are covered in Fig. 7. In contrast, the variation of the nonlinear to linear frequency ratio has been plotted against the vibration amplitude. Also, this plot shows a rising trend in which the nonlinear to linear frequency ratio is experiencing an increase by
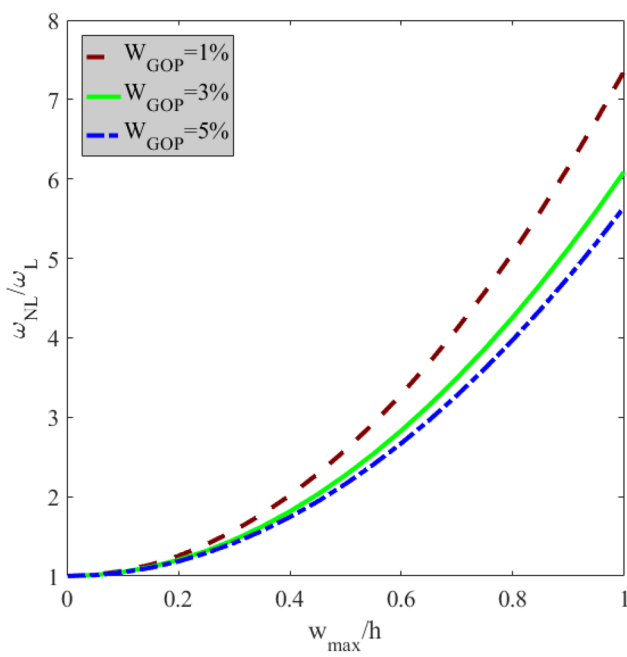
(a) h=0.002R
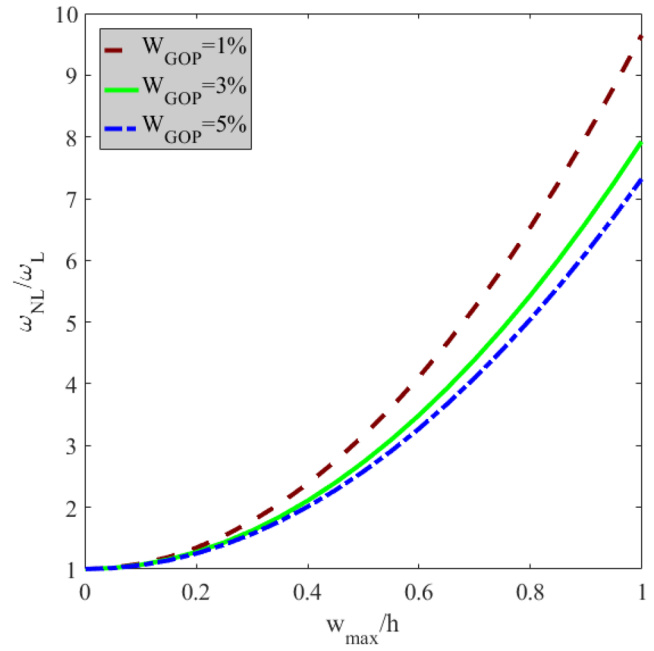
(b) h=0.0015R
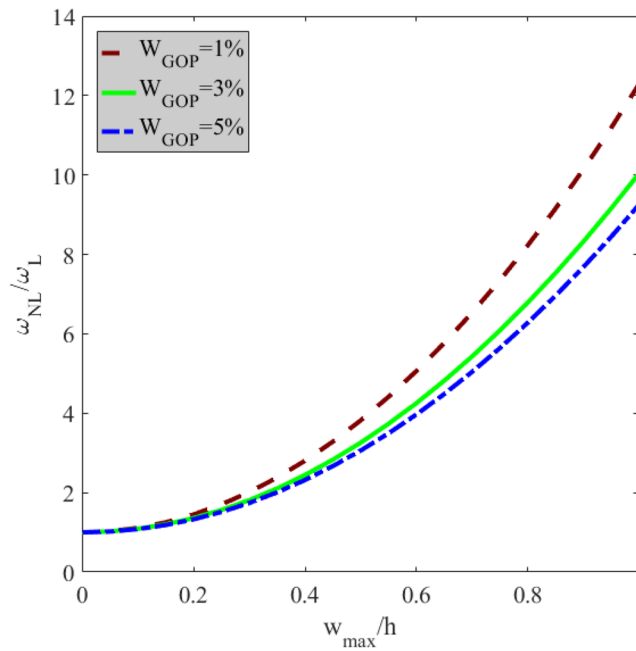
(c) h=0.001R

Fig. 7 Simultaneous effect of the GOPs' weight fraction and hybrid laminated nanocomposite cylindrical shell's length-to-radius ratio on the frequency ratio-amplitude curves ($m=1$, $n=3$, $V_{CF}=0.1$)

an increment in the vibration amplitude values. In addition, it is indicated that at any given value of the vibration amplitude parameter, an increment in the GOPs' weight fraction values leads to a reduction in the nonlinear to

linear frequency ratio values. It is worth noting that all of the reported outcomes are completely valid, as discussed in detail to declare logical and scientific reasons earlier.
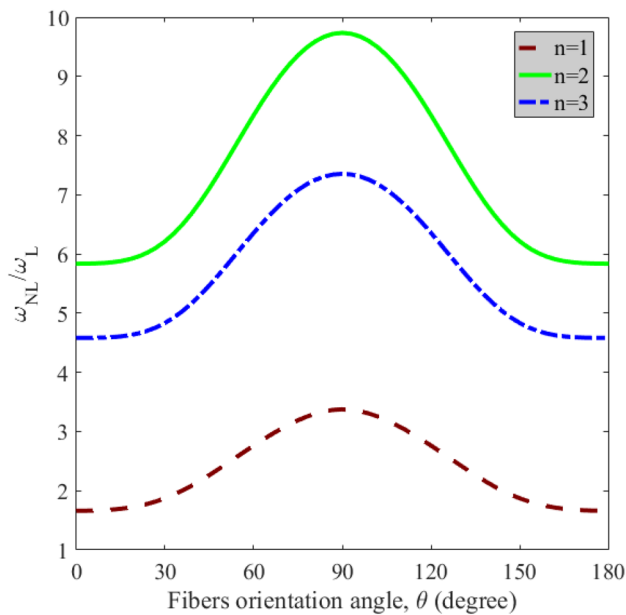
Fig. 8 Variation of the nonlinear to linear frequency ratio of the hybrid laminated nanocomposite cylindrical shell with considering various circumferential wave numbers ($m = 1$, $W_{GOP} = 1\%$, $V_{CF} = 0.1$, $\frac{w_{max}}{h} = 1$)

Furthermore, the length-to-radius ratio has a direct impact on the nonlinear to linear frequency ratio parameter in a way that an addition in the L/R parameter leads to an enhancement in the nonlinear to linear frequency ratios parameter.

Figure 8 is dedicated to investigating the variation of the nonlinear to linear frequency ratio of the hybrid laminated nanocomposite cylindrical shell based on the changes in the fibers' orientation angle parameter, considering disparate values of the circumferential wave number parameter. It can be perceived that the values of the nonlinear to linear frequency ratio are symmetrical with respect to the 90-degree fibers' orientation angle, and the maximum value of the mentioned under-study parameter appears at this angle of fibers' orientation. Also, around the 0- and 180-degree orientation angle, the nonlinear to linear frequency ratios values lead to a constant value symmetrically. Also, it is notable that at any given value of the fibers' orientation angle, the values of the nonlinear to linear frequency ratio increase by enhancement of the circumferential wavenumber parameter, up to reaching ($n = 2$), and then it experiences a reduction for the same scientific reason that discussed in former graphs (Fig. 6).

Conclusion

This article is primarily inquiring about the nonlinear frequency responses of the cross-ply laminated multi-scale hybrid nanocomposite shell embedded on a three-parameter nonlinear foundation. The macro-scale carbon fiber reinforcements are added to the polymer matrix, which is already reinforced with the nano-size GOPs. The homogenization procedure for deriving the effective material properties is conducted with an incorporation of the rule of mixture and Halpin–Tsai and methods. Also, an improved and more accurate form of the nonlinear Donnell's shell theory was introduced to predict the nonlinear strains' relations in a better way. Afterward, the nonlinear equations of motion are accomplished utilizing Hamilton's principle. Subsequently, to obtain the structure's natural frequencies, the derived nonlinear equations were analytically solved via a two-step process, including Galerkin and multiple-scale techniques. Finally, a complete parametric study was carried out in the framework of the nonlinear vibration analysis to cover both influences and confrontations of various parameters. Some of these new interesting consequences are expressed below.

- The increment of any kind of reinforcements, for instance, the weight fraction of the nano-size GOP or macro-scale CF reinforcement, and also nonlinear three-parameter foundation parameters, will improve the stiffness of the multi-scale hybrid nanocomposite.
- Improvement of stiffness undoubtedly increases the linear frequency parameter.
- Enhancement of stiffness characterization lessens the nonlinear to linear frequency ratio.
- The values of the nonlinear to linear frequency ratio increase by enhancement in the fibers' orientation angle, by approaching the 90-degree reaches the maximum value and then symmetrically, like the before-maximum value trend, lessens gradually and tends to a constant value.
- The values of the nonlinear to linear frequency ratio increase until reaching a particular maximum value and then decrease suddenly with varying slopes due to the enhancement of the circumferential wavenumbers.
- The growth in the radius to thickness ratio induces an increment in the nonlinear to linear frequency ratio values.
- The length-to-radius ratio values has a significant influence on the diagrams' trend of the nonlinear to linear frequency ratio due to the changes in fibers' orientation angle.

Appendix

$$\tilde{L}_{11} = -\frac{A_{11}m^2R^2\pi^2 + A_{66}n^2L^2}{\rho^T_{eff}L^2R^2},$$

$$\tilde{L}_{12} = \frac{(RA_{12} + RA_{66} + B_{12} + 2B_{66})mn\pi}{\rho^T_{eff}LR^2},$$

$$\tilde{L}_{13} = \frac{m\pi(L^2RA_{12} + m^2R^2\pi^2B_{11} + n^2L^2(B_{12} + 2B_{66}))}{\rho^T_{eff}L^3R^2},$$

$$\tilde{L}_{14} = 0,$$

$$\tilde{L}_{21} = \tilde{L}_{12},$$

$$\tilde{L}_{22} = -\frac{n^2L^2A_{11} + m^2R^2\pi^2A_{66} + (2n^2L^2/R)B_{22} + 4m^2R\pi^2B_{66} + n^2L^2D_{22} + 4m^2R^2\pi^2D_{66}}{\rho^T_{eff}L^2R^2},$$

$$\tilde{L}_{23} = -\frac{n(m^2R^3\pi^2(B_{12} + 2B_{66}) + L^2R(B_{22} + RA_{22}) + L^2n^2(RB_{22} + D_{22}) + m^2\pi^2R^2(D_{12} + 4D_{66}))}{\rho^T_{eff}L^2R^4},$$

$$\tilde{L}_{24} = 0,$$

$$\tilde{L}_{31} = \tilde{L}_{13},$$

$$\tilde{L}_{32} = \tilde{L}_{23},$$

$$\tilde{L}_{33} = \left[L^2R^2\left(-A_{22}L^2 + 2m^2\pi^2RB_{12} + 2(L^2n^2/R)B_{22} + n^2\left(L^2(-k_s) + m^2(-2D_{12} - 4D_{66})\pi^2\right)\right) - \left(L^2R^4\right)\left(k_LL^2 + m^2k_s\pi^2\right) - \left(D_{22}L^4n^4 + D_{11}m^4R^4\pi^4\right)\right]\Big/\rho^T_{eff}L^4R^4,$$

$$\tilde{L}_{34} = 0,$$

$$\tilde{L}_{35} = 0,$$

$$\tilde{L}_{36} = 0,$$

$$\tilde{L}_{37} = -\frac{9A_{11}(n^4L^4 + m^4R^4\pi^4) + 2(A_{12} + 2A_{66})m^2R^2\pi^2n^2L^2}{32\rho^T_{eff}L^4R^4}$$

Declarations

Conflict of Interest The authors declared no potential conflicts of interest with respect to the research, authorship, and/or publication of this article.

References

1. Botelho E, Rezende M, Lauke B (2003) Mechanical behavior of carbon fiber reinforced polyamide composites. Compos Sci Technol 63:1843–1855

2. Joshi SV, Drzal L, Mohanty A, Arora S (2004) Are natural fiber composites environmentally superior to glass fiber reinforced composites? Compos A Appl Sci Manuf 35:371–376

3. Cuppoletti J (2011) Nanocomposites and polymers with analytical methods, BoD–Books on Demand. InTech

4. Shen H-S, Xiang Y (2012) Nonlinear vibration of nanotube-reinforced composite cylindrical shells in thermal environments. Comput Methods Appl Mech Eng 213:196–205

5. Mirzaei M, Kiani Y (2015) Thermal buckling of temperature dependent FG-CNT reinforced composite conical shells. Aerosp Sci Technol 47:42–53

6. Heydarpour Y, Aghdam M, Malekzadeh P (2014) Free vibration analysis of rotating functionally graded carbon nanotube-reinforced composite truncated conical shells. Compos Struct 117:187–200

7. Heydari MM, Bidgoli AH, Golshani HR, Beygipoor G, Davoodi A (2015) Nonlinear bending analysis of functionally graded CNT-reinforced composite Mindlin polymeric temperature-dependent plate resting on orthotropic elastomeric medium using GDQM. Nonlinear Dyn 79:1425–1441

8. Chakraborty S, Dey T, Kumar R (2019) Stability and vibration analysis of CNT-Reinforced functionally graded laminated

composite cylindrical shell panels using semi-analytical approach. Compos B Eng 168:1–14

9. Avramov K, Chernobryvko M, Uspensky B, Seitkazenova K, Myrzaliyev D (2019) Self-sustained vibrations of functionally graded carbon nanotubes-reinforced composite cylindrical shells in supersonic flow. Nonlinear Dyn 98:1853–1876

10. Qin B, Zhong R, Wang T, Wang Q, Xu Y, Hu Z (2020) A unified Fourier series solution for vibration analysis of FG-CNTRC cylindrical, conical shells and annular plates with arbitrary boundary conditions. Compos Struct 232:111549

11. Liew K, Alibeigloo A (2021) Predicting bucking and vibration behaviors of functionally graded carbon nanotube reinforced composite cylindrical panels with three-dimensional flexibilities. Compos Struct 256:113039

12. Mahesh V (2021) Nonlinear damped transient vibrations of carbon nanotube-reinforced magneto-electro-elastic shells with different electromagnetic circuits. J Vib Eng Technol. https://doi.org/10.1007/s42417-021-00380-0

13. Gonçalves EH, Ribeiro P (2021) Modes of vibration of single-and double-walled CNTs with an attached mass by a nonlocal shell model. J Vib Eng Technol. https://doi.org/10.1007/s42417-021-00381-z

14. Yang Y, Lin Q, Guo R (2020) Axisymmetric wave propagation behavior in fluid-conveying carbon nanotubes based on nonlocal fluid dynamics and nonlocal strain gradient theory. J Vib Eng Technol. https://doi.org/10.1007/s42417-019-00194-1

15. Banerjee S, Sardar M, Gayathri N, Tyagi A, Raj B (2006) Enhanced conductivity in graphene layers and at their edges. Appl Phys Lett 88:062111

16. Novoselov KS, Jiang D, Schedin F, Booth T, Khotkevich V, Morozov S, Geim AK (2005) Two-dimensional atomic crystals. Proc Natl Acad Sci 102:10451–10453

17. Reddy C, Rajendran S, Liew K (2006) Equilibrium configuration and continuum elastic properties of finite sized graphene. Nanotechnology 17:864

18. Hu K, Kulkarni DD, Choi I, Tsukruk VV (2014) Graphene-polymer nanocomposites for structural and functional applications. Prog Polym Sci 39:1934–1972

19. Potts JR, Dreyer DR, Bielawski CW, Ruoff RS (2011) Graphene-based polymer nanocomposites. Polymer 52:5–25

20. Stankovich S, Dikin DA, Dommett GH, Kohlhaas KM, Zimney EJ, Stach EA, Piner RD, Nguyen ST, Ruoff RS (2006) Graphene-based composite materials. Nature 442:282–286

21. Scarpa F, Adhikari S, Phani AS (2009) Effective elastic mechanical properties of single layer graphene sheets. Nanotechnology 20:065709

22. Zhang Y, Wang C, Cheng Y, Xiang Y (2011) Mechanical properties of bilayer graphene sheets coupled by sp3 bonding. Carbon 49:4511–4517

23. Shen H-S, Lin F, Xiang Y (2017) Nonlinear vibration of functionally graded graphene-reinforced composite laminated beams resting on elastic foundations in thermal environments. Nonlinear Dyn 90:899–914

24. Li Q, Wu D, Chen X, Liu L, Yu Y, Gao W (2018) Nonlinear vibration and dynamic buckling analyses of sandwich functionally graded porous plate with graphene platelet reinforcement resting on Winkler-Pasternak elastic foundation. Int J Mech Sci 148:596–610

25. Ye C, Wang YQ (2021) Nonlinear forced vibration of functionally graded graphene platelet-reinforced metal foam cylindrical shells: internal resonances. Nonlinear Dyn 104(3):2051–2069

26. Stankovich S, Dikin DA, Piner RD, Kohlhaas KA, Kleinhammes A, Jia Y, Wu Y, Nguyen ST, Ruoff RS (2007) Synthesis of graphene-based nanosheets via chemical reduction of exfoliated graphite oxide. Carbon 45:1558–1565

27. Ramanathan T, Abdala A, Stankovich S, Dikin D, Herrera-Alonso M, Piner R, Adamson D, Schniepp H, Chen X, Ruoff R (2008) Functionalized graphene sheets for polymer nanocomposites. Nat Nanotechnol 3:327–331

28. Zhang Z, Li Y, Wu H, Zhang H, Wu H, Jiang S, Chai G (2020) Mechanical analysis of functionally graded graphene oxide-reinforced composite beams based on the first-order shear deformation theory. Mech Adv Mater Struct 27:3–11

29. Ebrahimi F, Nouraei M, Dabbagh A (2020) Thermal vibration analysis of embedded graphene oxide powder-reinforced nanocomposite plates. Engineering with Computers 36:879–895

30. Ebrahimi F, Nouraei M, Dabbagh A (2020) Modeling vibration behavior of embedded graphene oxide powder-reinforced nanocomposite plates in thermal environment. Mech Based Des Struct Mach 48:217–240

31. Ebrahimi F, Nouraei M, Dabbagh A, Civalek O (2019) Buckling analysis of graphene oxide powder-reinforced nanocomposite beams subjected to non-uniform magnetic field. Struct Eng Mech 71:351–361

32. Ebrahimi F, Nouraei M, Dabbagh A, Rabczuk T (2019) Thermal buckling analysis of embedded graphene-oxide powder-reinforced nanocomposite plates. Adv Nano Res 7:293–310

33. Ebrahimi F, Nouraei M, Seyfi A (2022) Wave dispersion characteristics of thermally excited graphene oxide powder-reinforced nanocomposite plates. Waves Random Complex Media 32:204–232

34. Wang Y, Zhou A, Xie K, Fu T, Shi C (2020) Nonlinear static behaviors of functionally graded polymer-based circular microarches reinforced by graphene oxide nanofillers. Results Phys 16:102894

35. Zarei MS, Azizkhani MB, Hajmohammad MH, Kolahch R (2017) Dynamic buckling of polymer–carbon nanotube–fiber multiphase nanocomposite viscoelastic laminated conical shells in hygrothermal environments. J Sandw Struct Mater. https://doi.org/10.1177/1099636217743288

36. Hajmohammad MH, Azizkhani MB, Kolahchi R (2018) Multiphase nanocomposite viscoelastic laminated conical shells subjected to magneto-hygrothermal loads: dynamic buckling analysis. Int J Mech Sci 137:205–213

37. Ebrahimi F, Seyfi A (2021) Wave propagation response of multi-scale hybrid nanocomposite shell by considering aggregation effect of CNTs. Mech Based Des Struct Mach 49:59–80

38. Ebrahimi F, Seyfi A (2022) Wave propagation response of agglomerated multi-scale hybrid nanocomposite plates. Waves Random Complex Media 32:1338–1362

39. Ebrahimi F, Seyfi A, Dabbagh A (2019) Wave dispersion characteristics of agglomerated multi-scale hybrid nanocomposite beams. J Strain Anal Eng Des 54:276–289

40. Nouraei M, Haghi P, Ebrahimi F (2021) Modeling dynamic characteristics of the thermally affected embedded laminated nanocomposite beam containing multi-scale hybrid reinforcement. Waves n Random Complex Media. https://doi.org/10.1080/17455030.2021.1988758

41. Yousefi AH, Memarzadeh P, Afshari H, Hosseini SJ (2020) Agglomeration effects on free vibration characteristics of three-phase CNT/polymer/fiber laminated truncated conical shells. Thin-Walled Struct 157:107077

42. Lee S-Y (2020) Dynamic stability and nonlinear transient behaviors of CNT-reinforced fiber/polymer composite cylindrical panels with delamination around a cutout. Nonlinear Dyn. https://doi.org/10.1007/s11071-020-05477-x

43. Shahmohammadi MA, Azhari M, Saadatpour MM, Salehipour H, Civalek Ö (2021) Dynamic instability analysis of general shells reinforced with polymeric matrix and carbon fibers using a coupled IG-SFSM formulation. Compos Struct 263:113720

44. Ebrahimi F, Habibi S (2018) Nonlinear eccentric low-velocity impact response of a polymer-carbon nanotube-fiber multiscale nanocomposite plate resting on elastic foundations in hygrothermal environments. Mech Adv Mater Struct 25:425–438

45. Soedel W, Qatu MS (2005) Vibrations of shells and plates. Acoustical Society of America. CRC Press

46. Amabili M (2008) Nonlinear vibrations and stability of shells and plates. Cambridge University Press

47. Li X, Du C, Li Y (2018) Parametric resonance of a FG cylindrical thin shell with periodic rotating angular speeds in thermal environment. Appl Math Model 59:393–409

48. Hao-nan L, Cheng L, Ji-ping S, Lin-quan Y (2021) Vibration analysis of rotating functionally graded piezoelectric nanobeams based on the nonlocal elasticity theory. J Vib Eng Technol. https://doi.org/10.1007/s42417-021-00288-9

49. Wang Y, Ye C, Zu J (2018) Identifying the temperature effect on the vibrations of functionally graded cylindrical shells with porosities. Appl Math Mech 39:1587–1604

50. Gonçalves PB, Ramos NR (1997) Numerical method for vibration analysis of cylindrical shells. J Eng Mech 123:544–550

51. Dym CL (1973) Some new results for the vibrations of circular cylinders. J Sound Vib 29:189–205

52. Raju KK, Rao GV (1976) Large amplitude asymmetric vibrations of some thin shells of revolution. J Sound Vib 44:327–333

53. Rafiee M, Mohammadi M, Aragh BS, Yaghoobi H (2013) Nonlinear free and forced thermo-electro-aero-elastic vibration and dynamic response of piezoelectric functionally graded laminated composite shells, part i: theory and analytical solutions. Compos Struct 103:179–187